Reflection Mechanism of Dielectric Corner Reflectors: The Role of the Diffraction of Evanescent Waves and the Goos−Hänchen Shift

Kishin Matsumori,* Ryushi Fujimura, and Markus Retsch

Read Online

ACCESS | Metrics & More | Article Recommendations | Supporting Information

ABSTRACT: Nano- and microstructures have been developed for asymmetric light transmission (ALT) filters operating in a wide wavelength range. One of the most straightforward structures with ALT properties is a dielectric corner reflector (DCR) comprising a one-dimensional grating of a triangular shape on one surface. The DCR possesses strong reflection only for one-way light illumination due to multiple total internal reflections (TIRs) inside the triangular grating. For triangular structures being much larger than the wavelength of light, the reflection properties are expected to be fully described by geometrical optics. However, geometrical optics do not account for the Goos−Hänchen (GH) shift, which is caused by the evanescent wave of the TIR. In this work, the reflection mechanism of DCRs is elucidated using the finite element method and a quantitative model built by considering the GH shift. The reduction in reflection of the DCR is dominated by diffraction of the evanescent wave at the corner of the triangular structure. Our model is based on simple mathematics and can optimize the DCR geometry for applications addressing a wide wavelength range such as radiative cooling.
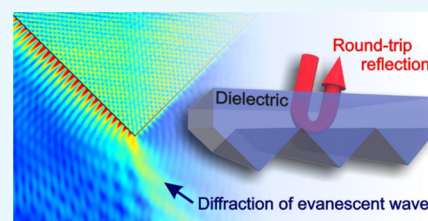
1. INTRODUCTION

Asymmetric light transmission (ALT) is an optical phenomenon in which transmission differs for forward and backward illumination of a device. ALT has been mainly investigated for optical communications, but it may be applied to advance energy applications, such as radiative cooling. Radiative cooling can passively cool down an object below the ambient temperature by emitting thermal radiation in the mid-infrared range (MIR) to the cold outer space.[1] However, under high humidity, it is known that the cooling performance is severely degraded since the thermal emission to outer space is attenuated, and an additional heat transfer between the emitter and the atmosphere needs to be considered.[2,3] Optical elements acting like ALT filters in the MIR range have recently been controversially discussed to counteract the cooling performance degradation under high humidity conditions. The fundamental idea of such a filter is to reflect the incoming atmospheric radiation while retaining the transmission of the outgoing thermal radiation.[4,5] An experimental proof of the feasibility of such a filter has not been shown, and a complete theoretical analysis is also missing, especially with a full description of the mode-to-mode conversion.[6,7] Further progress in this direction requires a thorough understanding of the optical properties of a suitable ALT filter, which, furthermore, should cover a broad wavelength range and work independently of the light polarization. Ultimately, for transitioning into a potential application, such an ALT filter needed to be simple and scalable to manufacture.

ALT can be achieved by optical non-reciprocity,[8−11] planar chiral structures,[12,13] photonic crystals,[14,15] and hyperbolic metamaterials.[16] Those structures can show a high performance in ALT. However, they mainly operate only at a specific wavelength. Widening the operational wavelength of ALT has been achieved by designing grating structures.[17−19] The ALT of grating structures is attributed to a difference in diffraction modes for the forward and backward illuminations. In this case, the intensity of zeroth-order transmission is the same for both illuminations, limiting ALT performance. In addition, their structure requires precise control of the periodicity of the grating, which makes it challenging to produce a scalable device. A dielectric microsphere whose top is partially covered by a perfect light absorber has been proposed as an ALT structure with a more straightforward fabrication process.[20] The microsphere acts as a ball lens, which focuses the incoming light on one point. This focused light is absorbed by the perfect absorber, resulting in low transmission only for one way. The operational wavelength range of ALT can be controlled by adjusting the size of the microsphere. This ALT is not attributed to a diffraction mode at all. Therefore, the periodicity of the microspheres is not essential, providing a considerable fabrication tolerance. However, light absorption is not desirable for radiative cooling because light absorption
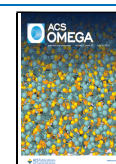
increases the temperature of a system, which causes degradation in cooling performance.

One alternative structure for broadband ALT is a dielectric corner reflector (DCR).[5,21] The DCR is a film with a one-dimensional grating of a triangular structure. The DCR is composed of a relatively simple microstructure that can be made of a low-cost polymer by a mechanical stamping,[22] enabling the production of large-area devices. The DCR can have high reflectance only when the light propagates into the DCR from the flat side. This is because a round-trip reflection, in which the light is reflected multiple times and its propagation direction is redirected backward, is made inside the triangular structure. The round-trip reflection is attributed to total internal reflections (TIRs) occurring at the surfaces of the triangular structure. The ALT of the DCR does not rely on either diffraction modes of the grating or light absorption. Therefore, a high-performance ALT for radiative cooling can be achieved. From a geometrical optics point of view, it is expected that the DCR can possess nearly perfect reflection in the MIR region by designing a triangular structure much larger than the wavelength. This is because the surfaces of the triangular structure can act as a reflective surface by TIR comparable to metallic surfaces. However, the reflectance of the DCR linearly decreases with an increase in the wavelength. This decrease occurs even though the triangular structure is sufficiently larger than the wavelength. Braginsky and Vyatchanin and Tarabrin suggested that evanescent waves created by TIRs could be diffracted at the downward corner of the triangular structure.[23,24] Therefore, the reflectance can decrease even within the geometrical optics regime. This diffraction loss was theoretically estimated; however, Braginsky and Vyatchanin and Tarabrin just considered the whole field around the surface of the triangular structure but did not consider directions of energy flux (EF) of the evanescent waves around the downward corner. In addition, their mathematical approach was too simplified compared to the diffraction of the evanescent wave created by the surface plasmon polaritons.[25,26] Therefore, their simple analysis may lose a lot of important information describing the diffraction loss mechanisms.

In this work, the reflection mechanism of a DCR is theoretically investigated by building a quantitative model to fundamentally understand the inherent reflection reduction. We build the model by considering the following: (1) part of the incident light is shifted outside of the DCR by the Goos–Hänchen (GH) shift and (2) the energy of the incident light shifted outside is lost by diffraction of the evanescent wave. Reflection spectra of the DCR estimated using our model are in good agreement with reflection spectra obtained using the finite element method (FEM). Electric field distribution maps obtained from the FEM simulation demonstrate that the diffraction of the evanescent wave occurs at the downward corner of the triangular structure. Our model suggests that this diffraction occurs no matter how large the DCR is relative to the wavelength. Our analysis is not confined to a specific wavelength range, which enables us to contribute to high-performance DCRs not only for radiative cooling but also for other applications requiring an ALT, such as silicon solar cells[27] and luminescent solar concentrators.[28]

2. GOOS–HÄNCHEN SHIFT

When the TIR reflects the light, the reflected light is laterally shifted from a point predicted by geometrical optics. This lateral shift is called the GH shift (Figure 1a). The amount of the shift was first formulated by Artmann.[29] He obtained the
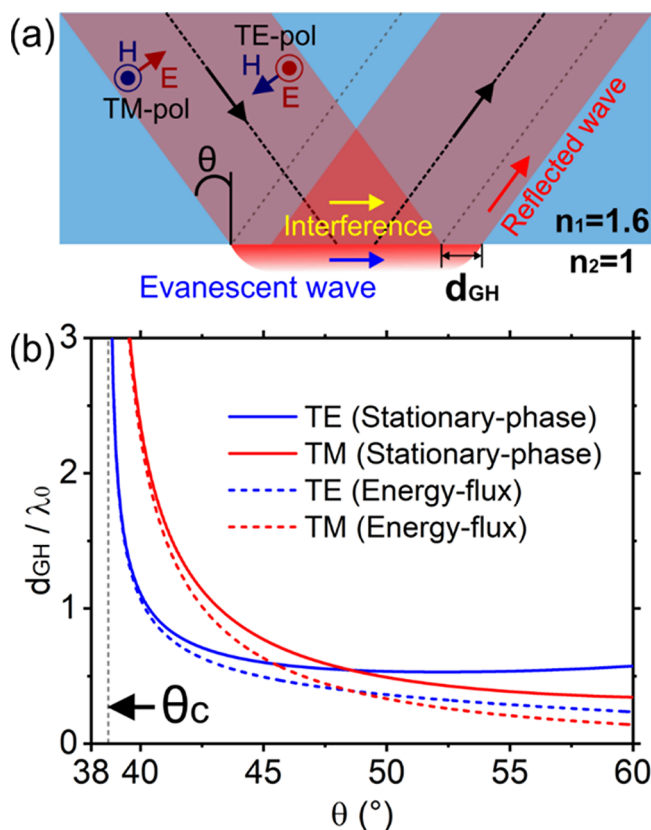

Figure 1. (a) Schematic illustration of the GH shift. The gray dashed lines show the reflected light path, predicted by geometrical optics. (b) GH shift calculated using the SP method and the EF method. The refractive indices of the optically denser and less dense medium are n_1 = 1.6 and n_2 = 1, respectively. The GH shift is normalized by the wavelength in vacuum.

GH shift by mathematically treating the phase difference between the incident and reflected lights. His stationary-phase (SP) method gives the GH shift for TE and TM polarizations as

$$d_{GH(SP)}^{TE} = \frac{\lambda_0}{\pi n_1} \frac{\tan \theta}{\sqrt{\sin^2 \theta - n^2}} \tag{1}$$

$$d_{GH(SP)}^{TM} = d_{GH(SP)}^{TE} \frac{n^2(1 - n^2)}{n^4 \cos^2 \theta + \sin^2 \theta - n^2} \tag{2}$$

where λ_0 is the wavelength in vacuum, θ is the incident angle, n is n_2/n_1, and n_1 and n_2 are refractive indices of an optically denser and less dense medium, respectively. Equations 1 and 2 are plotted in Figure 1b. After the SP method was proposed, Renard proposed an EF method.[30] This method is based on a consideration that the total EF of an evanescent wave created in an optically less dense medium (blue arrow in Figure 1a) must be conserved by the EF entering back into an optically denser medium (red arrow in Figure 1a). The EF method gives the GH shift as

$$d_{GH(EF)}^{TE} = \frac{\lambda_0}{\pi n_1} \frac{\sin \theta \cos \theta}{(1 - n^2)\sqrt{\sin^2 \theta - n^2}} \tag{3}$$
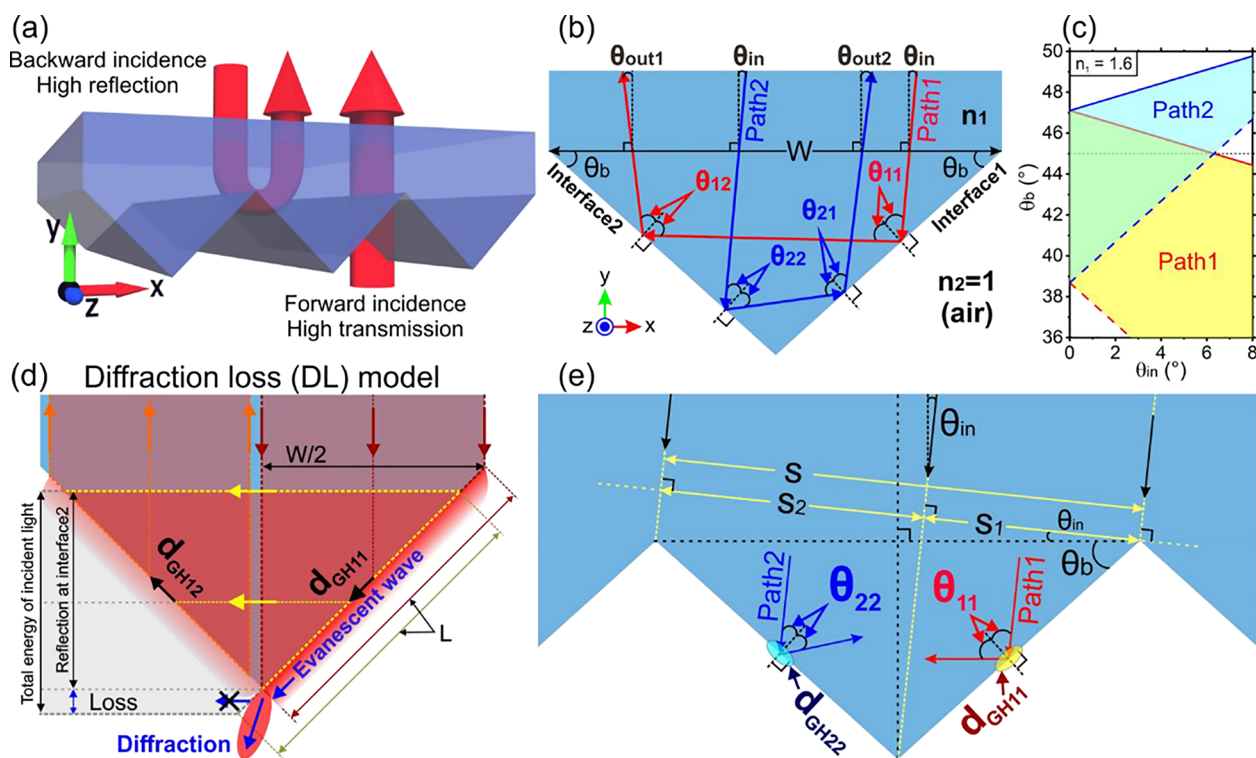
Figure 2. (a) Illustration of the DCR. (b) Schematic illustration of the cross-section of the DCR. The red and blue lines indicate the light paths inside the triangular structure. (c) Round-trip condition at oblique incidence for $n_1 = 1.6$. (d) Schematic illustration of the diffraction loss (DL) model. The red shaded area shows the light traveling along Path1 in (b). The dark red, yellow, and orange arrows indicate that the incident light strikes on Interface1, the light reflected at Interface1 and traveling to Interface2, and the light reflected at Interface2, respectively. The gray shaded area shows an imaginary path of the reflected light indicated by the yellow arrows if Interface1 was infinitely long and if there was no reflection at Interface2. (e) DL model for oblique incidence.

$$d_{GH(EF)}^{TM} = d_{GH(EF)}^{TE} \frac{n^2(1 - n^2)}{n^4 \cos^2 \theta + \sin^2 \theta - n^2} \tag{4}$$

Equations 3 and 4 are plotted in Figure 1b. It can be observed that there is a considerable discrepancy between the SP and EF methods at the incident angle far from the critical angle $\theta_c = \sin^{-1}(n_2/n_1)$. Yasumoto pointed out that this discrepancy occurs because the EF created by the interference between the incident and reflected light (yellow arrow in Figure 1a) is not considered in the EF method.[31] The GH shift calculated by considering both the evanescent wave and the interference coincides with the SP method.[31,32] At the incident angle close to θ_c, the GH shift is dominated by the EF of the evanescent wave. In contrast, when the incident angle is far from θ_c, the GH shift is dominated by the EF of the interference. Based on an understanding of the GH shift, we will investigate the reflection properties of the DCR.

3. DCRS IN GEOMETRICAL OPTICS AND NANO-OPTICS

3.1. Round-Trip Condition. Figure 2a shows a schematic of the DCR. We considered that the grating and triangular structures are infinitely large in the x- and z-direction, respectively. The forward incidence is that the light illuminates on the structured side. In this case, the DCR has high transmission. For the backward incidence, in which the light illuminates on the DCR from the flat side, the DCR can have a high reflectance by the round-trip reflection. Figure 2b shows the cross-section of one grating period, consisting of an isosceles triangular structure with a width W and a base angle

θ_b. In Figure 2b, two light paths inside the triangular structure are shown for backward incidence at the incident angle θ_{in}. For Path1, the light is reflected at Interface1 and goes to Interface2. Then, the light is reflected again at Interface2 and goes back to the flat side of the DCR. Path2 is in the opposite direction to Path1. We first consider the case of normal incidence, where $\theta_{in} = 0°$, to find the round-trip condition. In this case, Path1 and Path2 are now identical ($\theta_{11} = \theta_{22} = \theta_b$), meaning that only Path1 needs to be considered. The round-trip condition can be found using Snell's law and taking into account the incident angles at each interface, which are θ_{11} and θ_{12} (S1, Supporting Information).

$$\theta_c < \theta_b < \frac{180° - \theta_c}{3} \tag{5}$$

From the round-trip condition, a refractive index of the DCR n_1 should be larger than 1.42 when the surrounding of the DCR is the air. The minimum of the condition is determined by θ_c. For our study, $n_1 = 1.6$ is considered, which conventional polymers, such as polystyrene, possess.[33,34] In this case, θ_b can be in an angle range from 38.7 to 47.1° to satisfy the round-trip condition (Figure S1b, Supporting Information).

When the light is incident on the DCR at an oblique angle, we have to find round-trip conditions for Path1 and Path2 separately. Figure 2c shows the round-trip condition for the oblique incidence. The yellow and blue shaded areas indicate the round-trip conditions for Path1 and Path2, respectively. The round-trip condition for oblique incidence can be satisfied in the area where those two areas overlap each other (S1,
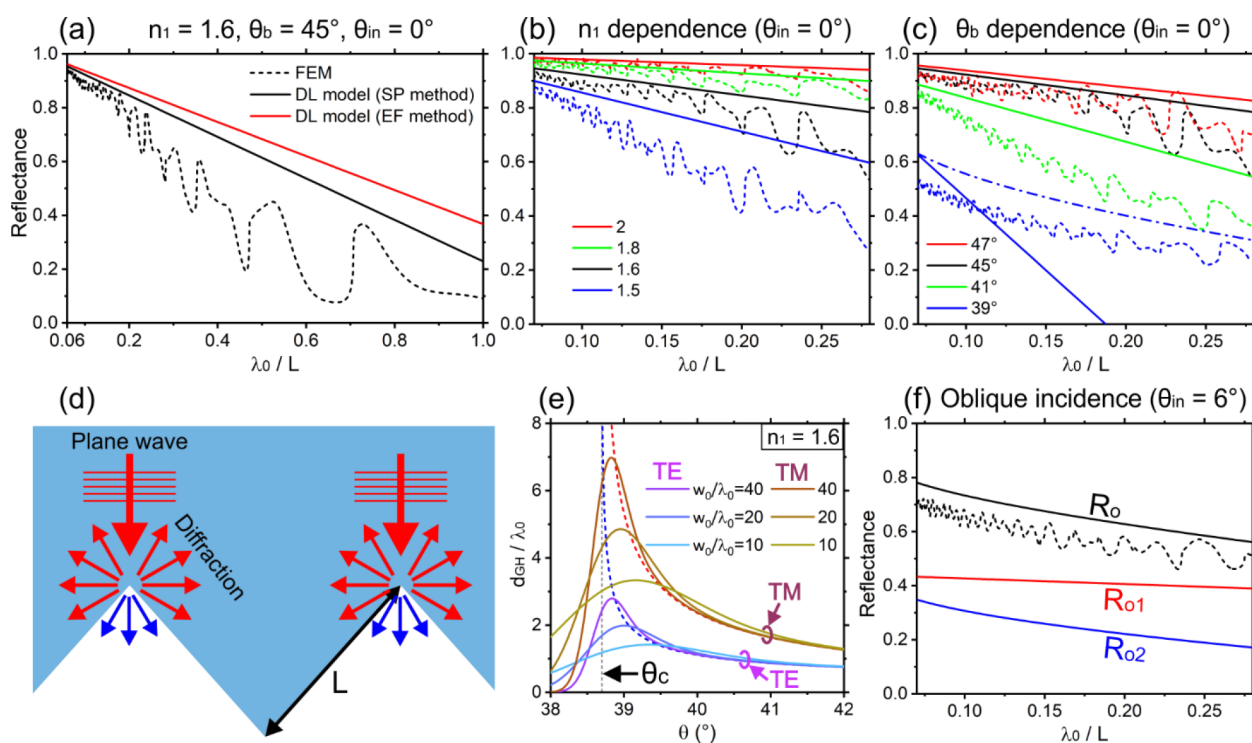
Figure 3. For (a−c), the dashed lines are reflection spectra calculated by the FEM simulation. The solid lines are calculated by the DL model (eq 6) using the SP method (eq 2). The incident light is TM polarized. Only backward incidence is considered. (a) Reflectance of the DCR with n_1 = 1.6 and θ_b = 45° at θ_{in} = 0°. The red solid line is calculated by the DL model using the EF method. (b) n_1 dependence. θ_b and θ_{in} are 45 and 0°, respectively. The red, green, black, and blue lines are for n_1 = 2, 1.8, 1.6, and 1.5, respectively. (c) θ_b dependence for the DCR with n_1 = 1.6 and θ_{in} = 0°. L is fixed and W changes according to θ_b. The red, black, green, and blue lines are for θ_b = 47, 45, 41, and 39°, respectively. The blue dashed–dotted line is calculated using the DL model with eq 9. w_0 is determined so that w_0/L becomes about 1.7. (d) Schematic illustration of the plane wave diffracted at the triangular structure's upward corners. (e) GH shift at around θ_c, which is given by eqs 8 and 9 for TE and TM polarizations. The blue and red dashed lines are the SP method, found in Figure 1b. (f) Reflection spectra for n_1 = 1.6, θ_b = 45°, and θ_{in} = 6°. The reflection spectra obtained from the DL model for Path1 (R_{o1}) and Path2 (R_{o2}) are the red and blue lines, respectively. R_{o1} and R_{o2} are calculated using eq 7 with eq 2 and with eq 9, respectively. The black solid is the sum of the red and blue solid lines.

Supporting Information). When θ_b is 45°, the round-trip reflection can occur at an incident angle up to about 6° for n_1 = 1.6. In the experimental system, the refraction at the flat surface of the DCR has to be taken into account. In this case, the condition can be satisfied up to the incident angle of 10° (Figure S3b, Supporting Information). For simplicity, the flat surface of the DCR is ignored, and this refraction is not considered in further theoretical investigations. The propagation direction of the light after the round-trip reflection, denoted by θ_{out} in Figure 2b, can be found in S1, Supporting Information. θ_{out} is equal to θ_{in} when θ_b is 45°, meaning that the DCR can act as a retroreflector.[35,36]

3.2. DL Model. By considering the GH shift and the geometry of the triangular structure, we investigate the reflection mechanism of the DCR in detail using Figure 2d. First, we only consider Path1 for normal incidence and assume that the plane wave strikes only one-half of the triangular structure (red arrows in Figure 2d). As mentioned earlier, the incident angle at Interface1 θ_{11} is equal to θ_b when θ_{in} = 0°. The center of the reflected light is laterally shifted on Interface1 by the GH shift d_{GH11}. However, Interface1 is not infinite. Therefore, the amount of the reflected light's energy, which is determined by the GH shift d_{GH11}, cannot completely come back into the structure (blue arrows in Figure 2d). According to the physical mechanism of the GH shift mentioned earlier, this energy is related to the evanescent wave propagating in the optically less dense medium. From the

research on propagating surface plasmon, it has been known that a propagating evanescent wave can be diffracted at the corner of the metal film.[25,26] A similar diffraction scenario is expected for the DCR because the evanescent wave still has an EF at the downward corner of the triangular structure. In addition, the EF created by the interference between the incident and reflected lights is also attributed to the GH shift. This amount of energy may also be diffracted at the downward corner. The rest of the incident light reaches Interface2 (yellow arrows in Figure 2d) and is reflected at Interface2 by the TIR (orange arrows in Figure 2d). The GH shift d_{GH12} occurs at Interface2, but the EF of either the evanescent wave or the interference is not toward the downward corner. Therefore, all the energy of the light reflected at Interface2 can go back into the triangular structure. Consequently, we expect a fraction of the incident energy to be lost by the diffraction governed by d_{GH11} during one cycle of the round-trip reflection. The same process happens for Path2. From this diffraction loss (DL) model, the reflectance of the DCR can be estimated by using the ratio of d_{GH11} to the side length of the triangular structure L. The DL model gives the reflectance of the DCR for normal incidence as

$$R_n = 1 - \frac{d_{GH11}}{L} \qquad (6)$$

For oblique incidence, a different amount of energy is lost during the round-trip reflection in Path1 and Path2 because

the incident angles $\theta_{11} = \theta_b + \theta_{in}$ and $\theta_{22} = \theta_b - \theta_{in}$ are different, resulting in $d_{GH11} \neq d_{GH22}$. When light is normally incident on the DCR, the energy of the incident light on Interface1 is equal to that on Interface2. However, for oblique incidence, the energy of the incident light striking on Interface1 and Interface2 is different (Figure 2e). This has to be taken into account in the DL model by considering the cross-section of the incident light entering a single triangular structure. The cross-section of the incident light can be expressed as $s = W\cos\theta_{in}$. The cross-section of the incident light that goes to Interface1 is $s_1 = L\cos(\theta_b + \theta_{in})$, and the rest goes to Interface2. Therefore, the reflectance of the DCR for oblique incidence can be estimated by

$$R_o = R_{o1} + R_{o2} = \frac{s_1}{s}\left(1 - \frac{d_{GH11}}{L}\right) + \frac{s_2}{s}\left(1 - \frac{d_{GH22}}{L}\right) \tag{7}$$

where R_{o1} and R_{o2} are the reflectance for Path1 and Path2, respectively. Equation 7 coincides with eq 6 when $\theta_{in} = 0°$. The DL model shows that a lossless reflection cannot be obtained because the GH shift cannot be zero even if the triangular structure was sufficiently larger than the wavelength. It has to be mentioned that, for Path2, part of the light reflected at Interface2 (R_{22}) does not strike on Interface1. However, R_{22} points to the flat top surface of the DCR. Therefore, R_{22} is not lost and is counted in the total reflectance of the DCR (S1, Supporting Information).

4. RESULTS AND DISCUSSION

4.1. DL Model with SP and EF Methods. We investigate the reflection properties of the DCR for backward incidence with TM polarization using the FEM (see Section 6). In this investigation, reflection and refraction occurring at the flat top surface of the DCR are ignored. We also use the DL model to gain insight into the reflection mechanism of the DCR. Reflection spectra are plotted as a function of the normalized unit of λ_0/L.

First, we compare the DL model (eq 6) with the SP method (eq 2) and that with the EF method (eq 4) to understand which method can properly describe the reflection of the DCR. Figure 3a shows the reflection spectra of the DCR with $n_1 = 1.6$ and $\theta_b = 45°$ at the incident angle of $\theta_{in} = 0°$. The dashed lines are spectra calculated by the FEM simulation. The black and red solid lines are calculated using the DL model with the SP and EF methods, respectively. There is a difference in spectral shape between the FEM and the DL model because the FEM considers the grating effect,[21] but the DL model does not. In terms of how reflectance decreases with an increase in the wavelength, it can be found that the DL model with the SP method is in good agreement with the FEM simulation. When the EF method is used in the DL model, the reflectance is slightly overestimated, indicating that the evanescent wave's energy and the energy created by the interference are lost by diffraction. From this result, we use only the SP method for further investigations.

4.2. λ_0/L and n_1 Dependencies. The reflectance of the FEM approximately linearly decreases with an increase in the wavelength for a fixed L (Figure 3a). Our DL model indicates that this linear decrease in reflectance is attributed to the GH shift being proportional to the wavelength. For a fixed λ_0, the reflectance can be higher for a large L since the reflection reduction of the DCR is inversely proportional to L (eq 6). We

are interested in the high reflectance of the DCR; therefore, we focus on a region of λ_0/L in which the reflectance can exceed 80%. In Figure 3b, the n_1 dependence of the reflection of the DCR is examined by changing n_1 in a range where the round-trip condition is satisfied. For those spectra, other parameters are fixed as $\theta_b = 45°$ and $\theta_{in} = 0°$. The DL model shows a good agreement with the FEM for all n_1. Since the GH shift is small for large n_1 and less energy is lost by the diffraction, the reflectance is higher when n_1 is larger. From the λ_0/L and n_1 dependencies, we conclude that a DCR with large L and large n_1 can possess strong reflection. However, an increase in L increases the size of the structure, which is undesirable for some applications requiring a compact system. In addition, increasing n_1 is not straightforward in experimental systems.[37] Therefore, it is required to find an optimum combination of L and n_1 to achieve a high-performance DCR.

4.3. θ_b Dependence. Figure 3c shows reflection spectra calculated for different θ_b with $n_1 = 1.6$ and $\theta_{in} = 0°$. For this calculation, L is fixed, and W is changed with the change in θ_b. The GH shift decreases with an increase in the incident angle (Figure 1b) so that the DCR with higher θ_b can possess a higher reflectance. However, the round-trip condition can be satisfied in a smaller incident angle range for larger θ_b (Figure 2c); therefore, there is a trade-off between higher reflectance and the incident angle insensitivity. This trade-off can be compensated just by increasing L. When θ_b is larger, the DL model shows good agreement with the FEM. However, the DL model cannot reproduce the results from the FEM when θ_b is close to θ_c. This is because neither the SP nor the EF methods can explain the GH shift around θ_c.

4.4. Influence of the GH Shift around θ_c. The GH shifts derived by eqs 1−4 diverge at θ_c (Figure 1b). However, when the incident light is a beam, such as a Gaussian beam, the GH shift has a maximum value at slightly greater than θ_c because of angular distribution in wave vector components of the incident beam. In the case of the DCR, we consider a plane wave as the incident light. In this case, diffraction occurs when the light strikes on the upward corners of the DCR (Figure 3d).[38] Therefore, the incident light on the triangular structure's surfaces is no longer a plane wave. The GH shift around θ_c was formulated using the Weber function[39,40] or modified Bessel function[41] for the Gaussian beam. Using the modified Bessel function,[41] the GH shift for TE and TM polarizations is

$$d_{GH(CA)}^{TE} = \frac{1}{\cos\theta}\sqrt{\frac{\pi\tan\theta}{2\sqrt{2}\,n_1}}\,S\left[\frac{kw_0\sigma_0}{2\sqrt{2}}\right]\sqrt{\frac{w_0}{k}} \tag{8}$$

$$d_{GH(CA)}^{TM} = \frac{d_{GH(CA)}^{TE}}{n_1^2\sin^2\theta - \cos^2\theta} \tag{9}$$

where

$$\sigma_0 = \frac{1 - n_1^2\sin^2\theta}{n_1\sin 2\theta}$$

$$S[x] = e^{-x^2}\sqrt{|x|}\,[I_{-1/4}(x^2) - \mathrm{sgn}(x)I_{1/4}(x^2)]$$

w_0 is the beam waist of the Gaussian beam, k is the angular wavenumber expressed as $2\pi/\lambda_0$, and $I_v(x)$ is the modified Bessel function of the first kind. Equations 8 and 9 hold in a limitation of $kw_0 \gg 1$. Equations 8 and 9 are plotted in Figure 3e for different ratios of w_0/λ_0. Compared to the SP method, those equations have a different line shape around θ_c but
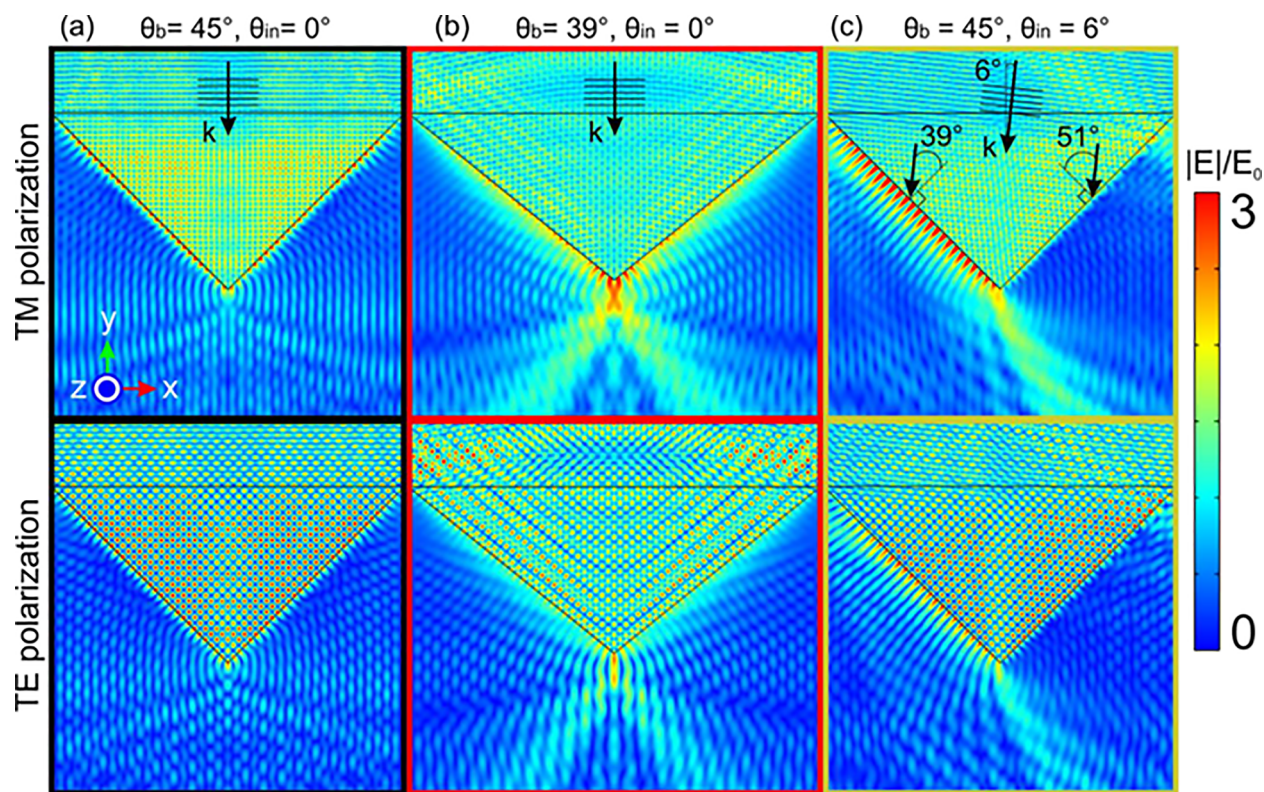
Figure 4. Color maps of the absolute value of electric field distribution at $\lambda_0/L \approx 0.07$ for (a) $\theta_b = 45°$ and $\theta_{in} = 0°$, (b) $\theta_b = 39°$ and $\theta_{in} = 0°$, and (c) $\theta_b = 45°$ and $\theta_{in} = 6°$. n_1 and n_2 are 1.6 and 1, respectively. The incident light is (top row) TM and (bottom row) TE polarized.

coincide with the SP method at the incident angle far from θ_c. With a decrease in w_0/λ_0, the maximum of the GH shift decreases and slightly shifts to a larger θ. Since the GH shift around θ_c is influenced by the angular distribution of wave vector components, the diffraction pattern at the upward corners of the DCR has to be carefully investigated for detailed analysis. However, for our phenomenological investigation, we use eqs 8 and 9 because the GH shift at around θ_c shows a similar line shape for different angular distributions, for example, for the case of the single-slit diffraction beam.[40,41] The beam waist determines the angular distribution of wave vector components in the Gaussian beam, so we use w_0 as a parameter that determines the diffraction pattern of the upward corners of the triangular structure.

In Figure 3c, the blue dashed−dotted line shows the reflection spectra estimated by the DL model using eq 9 with w_0 determined by $w_0/L \approx 1.7$. In this case, the DL model shows a similar trend to the FEM. We can understand why the reflectance does not linearly decrease for $\theta_b = 39°$ by considering the wavelength dependence of plane wave diffraction at the upward corners. Diffraction is weaker for smaller wavelengths, resulting in a larger GH shift. However, diffraction becomes stronger for longer wavelengths, and the GH shift becomes smaller. Therefore, the slope of the reflection spectrum is steeper in the shorter wavelength range, but the slope becomes gradually less steep with an increase in the wavelength.

4.5. Oblique Incidence. Considering the GH shift around θ_c, the reflection properties of the DCR at oblique incidence are investigated using the DL model in eq 7. Figure 3f shows the reflection spectrum of the DCR with $n_1 = 1.6$ and $\theta_b = 45°$. The incident angle is $\theta_{in} = 6°$, which is the upper limit of the

incident angle that can satisfy the round-trip condition (see Figure 2c). In this case, the incident light's energy on Interface1 and Interface2 is different, determined as $s_1/s \approx 0.45$ and $s_2/s \approx 0.55$, respectively. In addition, the incident angles at Interface1 for Path1 and at Interface2 for Path2 are different. The incident angle θ_{11} is 51° at Interface1 for Path1. θ_{11} is much larger than θ_c. Therefore, the SP method can be used for d_{GH11} in the DL model. The incident angle θ_{22} is 39° at Interface2 for Path2. θ_{22} is now close to θ_c, so d_{GH22} should be expressed using eq 9. w_0 is used again as a fitting parameter. When $w_0/L \approx 1.7$, the DL model shows good agreement with the FEM. For Path1, the reflectance linearly and slowly decreases with an increase in the wavelength because the GH shift is small for the incident angle of 51° (Figure 1b). For Path2, the reflectance decreases nonlinearly with an increase in the wavelength because θ_{22} is close to θ_c. The reflectance for Path1 is higher than that for Path2 even though $s_1/s < s_2/s$ because d_{GH11} is much smaller than d_{GH22}. Overall, our proposed DL model is robust for any combinations of the structural parameters of the DCR, and the DL model can consider the incident angle dependence of the DCR.

4.6. Polarization Dependence and Transmission for Forward Incidence. The same investigations are made for TE polarization (Figure S5, Supporting Information). The DL model also shows good agreement with the FEM for TE polarization. The DCR has the same reflection properties for TE and TM polarizations. The GH shift for TE polarization is smaller than that for TM polarization when the incident angle is smaller than about 48° (Figure 1b). Therefore, the reflectance is higher for TE polarization for normal incidence. For the DCR with θ_b close to θ_c, the same fitting made in Figure 3c was employed for TE polarization using w_0 as a

fitting parameter. The fitting resulted in $w_0/L \approx 3.5$, which is significantly different from that for TM polarization. To understand the physical meaning of those values, the polarization dependence of the diffraction pattern created by upward corners of the DCR has to be investigated in detail.[38]

Compared with TE polarization, the FEM and the DL model difference is larger for TM polarization for all reflection spectra. The diffraction at the upward corner may contribute to this discrepancy. Our analysis suggested that the value of w_0 can be smaller for TM polarization, meaning that the diffraction at the upward corner is more substantial for TM polarization. If the diffraction is strong, more incident light may go outside the DCR (blue arrows in Figure 3d), which the DL model does not consider.

The transmission properties of the DCR for the forward incidence can be found in Figure S7, Supporting Information. The transmission was calculated without taking the reflection and refraction at the flat surface of the DCR into account. The transmission is >90% for normal and oblique incidence for TM and TE polarizations. Since the DCR has a high reflectance for backward incidence, it can act as a high-performance broadband ALT filter in a specific incident angle range.

4.7. Diffraction of Evanescent Waves. For a better insight into the reflection mechanisms of the DCR, electric field distribution maps for TM and TE polarizations were obtained using the FEM. The top row of Figure 4 shows the field maps of the DCR with $n_1 = 1.6$ for TM polarization at $\lambda_0/L \approx 0.07$. For the DCR with $\theta_b = 45°$ and $\theta_{in} = 0°$ (Figure 4a), the electric field is confined inside the DCR, which attributes to the high reflectance. The GH shift for $\theta_b = 45°$ is not large, so the diffraction of the evanescent wave at the downward corner is not significant. Figure 4b shows the field map of the DCR with $\theta_b = 39°$. The incident angle is 0°. Compared to $\theta_b = 45°$, the electric field at the interfaces of the triangular structure is stronger because the penetration depth of the evanescent wave is larger for the incident angle close to θ_c. Interestingly, strong electric fields in the air region lower than the downward corner can be found. These fields are attributed to the diffraction of the evanescent wave. Figure 4c shows the field map for the DCR with $\theta_b = 45°$ and $\theta_{in} = 6°$. In this configuration, the incident angles at Interface1 and Interface2 are 51 and 39°, respectively. At interface1, the incident angle is much higher than θ_c, resulting in a weak evanescent wave. On the other hand, the incident angle at Interface2 is close to θ_c, so the evanescent wave is strong. Therefore, the diffraction of evanescent waves can be observed only along Interface2. This field map confirms why the reflectance is smaller for Path2, as shown in Figure 3f. The bottom row of Figure 4 shows the field maps for TE polarization, which are similar to those for TM polarization. This is because, as mentioned earlier, the DCR has almost the same reflection properties for both polarizations. The field maps at large λ_0/L can be found in S2, Supporting Information. In all cases, more energy of the incident light reaches outside of the triangular structure because the reflection reduction of the DCR is proportional to λ_0/L.

We must mention the diffraction of the EF created by the interference between incident and reflected lights, which cannot be observed in the field maps. Since the contribution of the interference on the GH shift is small compared to the evanescent wave (Figure 1b), we conclude that the diffraction of the evanescent wave dominates the reduction in reflection of the DCR. To understand the mechanism of diffraction loss by

the GH shift, a more detailed mathematical analysis is required by considering the EF of electromagnetic waves inside and outside the triangular structure.[42]

4.8. Optimization of the DCR. Next, we discuss how to optimize the DCR for high reflectance in a specific wavelength range using the DL model. As mentioned earlier, the reflectance of the DCR linearly decreases with increasing wavelength. Therefore, we only have to consider the reflectance at the maximum of the wavelength range λ_{max} to find an optimum size of the DCR. For example, if the DCR has to have a reflectance higher than 90% in a wavelength range shorter than λ_{max} for normal incidence and unpolarized light, we can find an optimum W of the DCR with arbitrary n_1 and θ_b using eq 6

$$1 - \frac{d_{GH(SP)}^{TE}|_{\lambda_0=\lambda_{max}} + d_{GH(SP)}^{TM}|_{\lambda_0=\lambda_{max}}}{2L} \geq 0.9 \tag{10}$$

Since the GH shift is large at around θ_c, a DCR with $\theta_b \approx \theta_c$ cannot possess a high reflectance. Also, the expression of the GH shift around θ_c is relatively complicated. Therefore, for simplicity, θ_b close to θ_c is not considered, and only the SP method is used in eq 10. From eq 10, when $n_2 = 1$, W should be

$$\frac{W}{\lambda_{max}} \geq \frac{10\sin\theta_b}{\pi\sqrt{n_1^2\sin^2\theta_b - 1}}\left(1 + \frac{1}{n_1^2\sin^2\theta_b - \cos^2\theta_b}\right) \tag{11}$$

$L = W/2\cos\theta_b$ was used to derive eq 11. Figure 5 shows eq 11 in the round-trip condition for normal incidence (eq 5). The
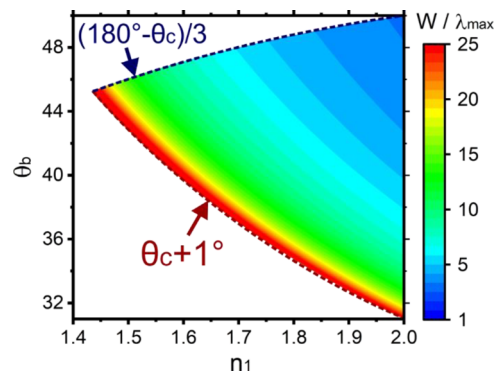

Figure 5. Size optimization of the DCR for reflectance higher than 90% in a wavelength range shorter than λ_{max}.

SP method diverges at θ_c, so eq 11 was calculated for θ_b larger than $\theta_c + 1°$. W/λ_{max} is smaller for larger n_1 and larger θ_b because the GH shift becomes smaller. The DCR can be optimized efficiently by determining n_1 and θ_b depending on applications and finding W from Figure 5. For radiative cooling, high reflectance in a wide incident angle range is expected so that 45° is an optimum angle for θ_b (Figure 2c). For example, in the case of $n_1 = 1.6$ and $\theta_b = 45°$, W/λ_{max} is 9.7. Since many polymers have a refractive index lower than 1.6,[33,34] it can be found that the DCR made of a polymer is required to be $W/\lambda_{max} > 9.7$ for reflectance higher than 90%. It should be mentioned that, as can be seen in Figure 3, the DL model slightly overestimates the reflectance of the DCR. Therefore, the DCR has to be slightly larger than the W estimated by eq 11.

Besides the structural optimization shown in Figure 5, a challenge for using such DCR structures as filters for radiative cooling applications is their sensitivity to the incident angle (Figure 2c). As outlined in the Section 1, the feasibility of their ALT properties is also controversially debated until now.[4−7] Our improved understanding of the reflection mechanism of a DCR enabled us to reassess their contribution to radiative cooling. Our simplified mode-to-mode conversion analysis indicates a potential positive effect (S3, Supporting Information). However, it also requires further analysis to take all contributions into account.

5. CONCLUSIONS

We have revealed the reflection mechanism of a DCR by using the DL model. From the DL model, we found that the reflectance of the DCR can be estimated just by considering the GH shift and the geometry of the triangular structure. The reflection spectra of the DCR were calculated using the FEM for different structural parameter combinations, which were compared with the spectra estimated by the DL model. Even though the DL model does not require any complicated mathematics, the DL model showed good agreement with the FEM. From the comparison, we revealed that the reflectance linearly decreases with an increase in the wavelength because the GH shift is proportional to the wavelength. We obtained the electric field distribution maps using the FEM and demonstrated that the diffraction of the evanescent wave occurs at the downward corner of the triangular structure. Since the GH shift does not become zero even though the triangular structure is significantly larger than the wavelength, this diffraction causes the intrinsic reflection reduction of the DCR.

In addition to radiative cooling, the DL model is useful to optimize the DCR efficiently for its potential applications, such as silicon solar cells,[27] luminescent solar concentrators,[28] non-contact temperature sensors,[22] and free-space optical communications.[43,44] Furthermore, our work may be essential to better understand light−matter interactions in other systems. For example, recently, coloration has been achieved by hemispherical dielectric microstructures.[45−47] The coloration is attributed to the round-trip reflection by TIRs and light interference occurring inside the microstructure. Geometrical optics explained this coloration mechanism. However, since TIR plays a pivotal role in this coloration mechanism, the GH shift and the diffraction of evanescent waves may also contribute to the reflected spectrum. Therefore, we expect that our DL model provides a deeper insight into the coloration mechanism of those microstructures.

6. METHOD

6.1. FEM Simulation. The optical properties of the DCR for the forward and backward incidence were investigated using COMSOL multiphysics, a commercial software package based on the FEM. The simulation model of the DCR was built in two dimensions. Figure 2b is a unit cell of the simulation model. The periodic boundary condition was applied to the x-direction to consider the infinitely long grating. The periodicity is the same as the width of the triangular structure. The film part of the DCR, which is on top of the triangular structure, was considered infinitely thick to remove noise from the Fabry−Perot resonance. The perfectly matched layers were applied on the top and bottom of the

model in the y-direction. To obtain total reflectance and transmittance, not only zeroth-order but also all higher-order diffraction modes were taken into account. The incident light is a plane wave with either TE (the electric field is along the z-direction) or TM (the magnetic field is along the z-direction) polarization.

ASSOCIATED CONTENT

Supporting Information

The Supporting Information is available free of charge at https://pubs.acs.org/doi/10.1021/acsomega.2c01537.

> Round-trip reflection for normal and oblique incidence; optical properties of the DCR; and mode-to-mode conversion of the DCR (PDF)

AUTHOR INFORMATION

Corresponding Author

Kishin Matsumori − *Department of Chemistry, Physical Chemistry I, University of Bayreuth, Bayreuth 95447, Germany;* orcid.org/0000-0002-5615-9032; Email: kishin.matsumori@uni-bayreuth.de

Authors

Ryushi Fujimura − *Graduate School of Regional Development and Creativity, Utsunomiya University, Utsunomiya 321-8585, Japan*

Markus Retsch − *Department of Chemistry, Physical Chemistry I, University of Bayreuth, Bayreuth 95447, Germany;* orcid.org/0000-0003-2629-8450

Complete contact information is available at:
https://pubs.acs.org/10.1021/acsomega.2c01537

Notes

The authors declare no competing financial interest.

REFERENCES

(1) Zhao, B.; Hu, M.; Ao, X.; Chen, N.; Pei, G. Radiative Cooling: A Review of Fundamentals, Materials, Applications, and Prospects. *Appl. Energy* **2019**, *236*, 489−513.

(2) Tso, C. Y.; Chan, K. C.; Chao, C. Y. H. A Field Investigation of Passive Radiative Cooling under Hong Kong's Climate. *Renew. Energy* **2017**, *106*, 52−61.

(3) Dong, M.; Chen, N.; Zhao, X.; Fan, S.; Chen, Z. Nighttime Radiative Cooling in Hot and Humid Climates. *Opt. Express* **2019**, *27*, 31587−31598.

(4) Wong, R. Y. M.; Tso, C. Y.; Chao, C. Y. H.; Huang, B.; Wan, M. P. Ultra-Broadband Asymmetric Transmission Metallic Gratings for Subtropical Passive Daytime Radiative Cooling. *Sol. Energy Mater. Sol. Cells* **2018**, *186*, 330−339.

(5) Wei, M.; Wu, W.; Li, D.; Xu, H.; Lu, Y.; Song, W. Universal Strategy for All-Weather and All-Terrain Radiative Cooling with Non-Reciprocal Mid-Infrared Windows. *Solar Energy* **2020**, *207*, 471−478.

(6) Wu, X.; Wang, C. The Application of Asymmetric Transmission in Daytime Radiative Cooling Cannot Increase the Cooling Power. *Sol. Energy Mater. Sol. Cells* **2020**, *215*, No. 110662.

(7) Ulpiani, G.; Ranzi, G.; Feng, J.; Santamouris, M. Expanding the Applicability of Daytime Radiative Cooling: Technological Developments and Limitations. *Energy Build.* **2021**, *243*, No. 110990.

(8) Khanikaev, A. B.; Mousavi, S. H.; Shvets, G.; Kivshar, Y. S. One-Way Extraordinary Optical Transmission and Nonreciprocal Spoof Plasmons. *Phys. Rev. Lett.* **2010**, *105*, No. 126804.

(9) Lawrence, M.; Barton, D. R., III; Dionne, J. A. Nonreciprocal Flat Optics with Silicon Metasurfaces. *Nano Lett.* **2018**, *18*, 1104−1109.

(10) Jalas, D.; Petrov, A.; Eich, M.; Freude, W.; Fan, S.; Yu, Z.; Baets, R.; Popović, M.; Melloni, A.; Joannopoulos, J. D.; Vanwolleghem, M.; Doerr, C. R.; Renner, H. What Is — and What Is Not — an Optical Isolator. *Nat. Photonics* **2013**, *7*, 579−582.

(11) Fan, S.; Baets, R.; Petrov, A.; Yu, Z.; Joannopoulos, J. D.; Freude, W.; Melloni, A.; Popović, M.; Vanwolleghem, M.; Jalas, D.; Eich, M.; Krause, M.; Renner, H.; Brinkmeyer, E.; Doerr, C. R. Comment on "Nonreciprocal Light Propagation in a Silicon Photonic Circuit". *Science* **2012**, *335*, 38 author reply 38.

(12) Schwanecke, A. S.; Fedotov, V. A.; Khardikov, V. V.; Prosvirnin, S. L.; Chen, Y.; Zheludev, N. I. Nanostructured Metal Film with Asymmetric Optical Transmission. *Nano Lett.* **2008**, *8*, 2940−2943.

(13) Singh, R.; Plum, E.; Menzel, C.; Rockstuhl, C.; Azad, A. K.; Cheville, R. A.; Lederer, F.; Zhang, W.; Zheludev, N. I. Terahertz Metamaterial with Asymmetric Transmission. *Phys. Rev. B* **2009**, *80*, No. 153104.

(14) Wang, C.; Zhou, C. Z.; Li, Z. Y. On-Chip Optical Diode Based on Silicon Photonic Crystal Heterojunctions. *Opt. Express* **2011**, *19*, 26948−26955.

(15) Wang, C.; Zhong, X. L.; Li, Z. Y. Linear and Passive Silicon Optical Isolator. *Sci. Rep.* **2012**, *2*, 674.

(16) Xu, T.; Lezec, H. J. Visible-Frequency Asymmetric Transmission Devices Incorporating a Hyperbolic Metamaterial. *Nat. Commun.* **2014**, *5*, 4141.

(17) Tang, B.; Li, Z.; Liu, Z.; Callewaert, F.; Aydin, K. Broadband Asymmetric Light Transmission through Tapered Metallic Gratings at Visible Frequencies. *Sci. Rep.* **2016**, *6*, 39166.

(18) Ozer, A.; Kocer, H.; Kurt, H. Broadband and Polarization-Independent Asymmetric Transmission of Visible Light through a Three-Dimensional Trapezoidal Metallic Metasurface. *J. Opt. Soc. Am. B* **2018**, *35*, 2111−2117.

(19) Zhu, R.; Wu, X.; Hou, Y.; Zheng, G.; Zhu, J.; Gao, F. Broadband Asymmetric Light Transmission at Metal/Dielectric Composite Grating. *Sci. Rep.* **2018**, *8*, 999.

(20) Ghobadi, A.; Dereshgi, S. A.; Butun, B.; Ozbay, E. Ultra-Broadband Asymmetric Light Transmission and Absorption through the Use of Metal Free Multilayer Capped Dielectric Microsphere Resonator. *Sci. Rep.* **2017**, *7*, 14538.

(21) Bose, G.; Vartiainen, I.; Roussey, M.; Kuittinen, M.; Tervo, J.; Turunen, J. Dielectric V-Ridge Gratings: Transition from Antireflection to Retroreflection. *Appl. Opt.* **2017**, *56*, 3004−3009.

(22) Khalid, M. W.; Ahmed, R.; Yetisen, A. K.; Butt, H. Flexible Corner Cube Retroreflector Array for Temperature and Strain Sensing. *RSC Adv.* **2018**, *8*, 7588−7598.

(23) Braginsky, V. B.; Vyatchanin, S. P. Corner Reflectors and Quantum-Non-Demolition Measurements in Gravitational Wave Antennae. *Phys. Lett. A* **2004**, *324*, 345−360.

(24) Tarabrin, S. P. An Approximate Analysis of the Diffraction Losses in Corner Reflectors. *Moscow Univ. Phys.* **2007**, *62*, 81−85.

(25) Zon, V. B. Reflection, Refraction, and Transformation into Photons of Surface Plasmons on a Metal Wedge. *J. Opt. Soc. Am. B* **2007**, *24*, 1960−1967.

(26) Kotelnikov, I. A.; Gerasimov, V. V.; Knyazev, B. A. Diffraction of a Surface Wave on a Conducting Rectangular Wedge. *Phys. Rev. A* **2013**, *87*, No. 023828.

(27) Gaucher, A.; Cattoni, A.; Dupuis, C.; Chen, W.; Cariou, R.; Foldyna, M.; Lalouat, L.; Drouard, E.; Seassal, C.; Roca i Cabarrocas, P.; Collin, S. Ultrathin Epitaxial Silicon Solar Cells with Inverted Nanopyramid Arrays for Efficient Light Trapping. *Nano Lett.* **2016**, *16*, 5358−5364.

(28) Oliveto, V.; Borca-Tasciuc, D.-A. Broadband Asymmetric Light Transmission Interfaces for Luminescent Solar Concentrators. *Nanoscale Adv.* **2021**, *3*, 3627−3633.

(29) Artmann, K. Berechnung Der Seitenversetzung Des Total-reflektierten Strahles. *Ann. Phys.* **1948**, *437*, 87−102.

(30) Renard, R. H. Total Reflection: A New Evaluation of the Goos−Hänchen Shift. *J. Opt. Soc. Am.* **1964**, *54*, 1190−1197.

(31) Yasumoto, K.; Ōishi, Y. A New Evaluation of the Goos−Hänchen Shift and Associated Time Delay. *J. Appl. Phys.* **1983**, *54*, 2170−2176.

(32) Chen, X.; Lu, X. J.; Zhao, P. L.; Zhu, Q. B. Energy Flux and Goos-Hanchen Shift in Frustrated Total Internal Reflection. *Opt. Lett.* **2012**, *37*, 1526−1528.

(33) Zhang, X.; Qiu, J.; Li, X.; Zhao, J.; Liu, L. Complex Refractive Indices Measurements of Polymers in Visible and near-Infrared Bands. *Appl. Opt.* **2020**, *59*, 2337−2344.

(34) Zhang, X.; Qiu, J.; Zhao, J.; Li, X.; Liu, L. Complex Refractive Indices Measurements of Polymers in Infrared Bands. *J. Quant. Spectrosc. Radiat. Transfer* **2020**, *252*, No. 107063.

(35) Lundvall, A.; Nikolajeff, F.; Lindstrom, T. High Performing Micromachined Retroreflector. *Opt. Express* **2003**, *11*, 2459−2473.

(36) Arbabi, A.; Arbabi, E.; Horie, Y.; Kamali, S. M.; Faraon, A. Planar Metasurface Retroreflector. *Nat. Photonics* **2017**, *11*, 415−420.

(37) Higashihara, T.; Ueda, M. Recent Progress in High Refractive Index Polymers. *Macromolecules* **2015**, *48*, 1915−1929.

(38) Gennarelli, G.; Riccio, G. Plane-Wave Diffraction by an Obtuse-Angled Dielectric Wedge. *J. Opt. Soc. Am. A* **2011**, *28*, 627−632.

(39) Horowitz, B. R.; Tamir, T. Lateral Displacement of a Light Beam at a Dielectric Interface. *J. Opt. Soc. Am.* **1971**, *61*, 586−594.

(40) Lai, H. M.; Cheng, F. C.; Tang, W. K. Goos−Hänchen Effect around and Off the Critical Angle. *J. Opt. Soc. Am. A* **1986**, *3*, 550−557.

(41) Araújo, M. P.; De Leo, S.; Maia, G. G. Closed-Form Expression for the Goos-Hänchen Lateral Displacement. *Phys. Rev. A* **2016**, *93*, No. 023801.

(42) Lai, H. M.; Kwok, C. W.; Loo, Y. W.; Xu, B. Y. Energy-Flux Pattern in the Goos-Hanchen Effect. *Phys. Rev. E* **2000**, *62*, 7330−7339.

(43) Jia, H.; Yin, H.; Zhang, H.; Wang, X.; Chang, S.; Yang, J. Study on the Heterodyning Scattering of Retroreflective Free-Space Optical Communication with Optical Heterodyning. *J. Opt. Soc. Am. A* **2013**, *30*, 2286−2290.

(44) Yang, G.; You, S.; Bi, M.; Fan, B.; Lu, Y.; Zhou, X.; Li, J.; Geng, H.; Wang, T. Wave-Optics Simulation of the Double-Pass Beam Propagation in Modulating Retro-Reflector Fso Systems Using a Corner Cube Reflector. *Appl. Opt.* **2017**, *56*, 7474−7483.

(45) Goodling, A. E.; Nagelberg, S.; Kaehr, B.; Meredith, C. H.; Cheon, S. I.; Saunders, A. P.; Kolle, M.; Zarzar, L. D. Colouration by Total Internal Reflection and Interference at Microscale Concave Interfaces. *Nature* **2019**, *566*, 523−527.

(46) Goodling, A. E.; Nagelberg, S.; Kolle, M.; Zarzar, L. D. Tunable and Responsive Structural Color from Polymeric Microstructured Surfaces Enabled by Interference of Totally Internally Reflected Light. *ACS Mater. Lett.* **2020**, *2*, 754−763.

(47) Li, K.; Li, T.; Zhang, T.; Li, H.; Li, A.; Li, Z.; Lai, X.; Hou, X.; Wang, Y.; Shi, L.; Li, M.; Song, Y. Facile Full-Color Printing with a Single Transparent Ink. *Sci. Adv.* **2021**, *7*, No. eabh1992.